Construction of Nitrogen-abundant Graphyne Scaffolds via Mechanochemistry-Promoted Cross-linking of Aromatic Nitriles with Carbide Towards Enhanced Energy Storage

Juntian Fan, Tao Wang, Bishnu P. Thapaliya, Meijia Li, Chi-Linh Do-Thanh, Takeshi Kobayashi, Ilja Popovs, Zhenzhen Yang*, and Sheng Dai*

J. Fan, Dr. C.-L. Do-Thanh, Dr. S. Dai

Department of Chemistry, Institute for Advanced Materials and Manufacturing, University of Tennessee, Knoxville, TN 37996, USA

Dr. T. Wang, Dr. B. P. Thapaliya, Dr. M. Li, Dr. I. Popovs, Dr. Z. Yang, Dr. S. Dai

Chemical Sciences Division, Oak Ridge National Laboratory, Oak Ridge, TN 37831, USA

Dr. T. Kobayashi

U.S. DoE Ames Laboratory, Iowa State University, Ames, IA 50011, USA

E-mail: yangz3@ornl.gov, dais@ornl.gov

Abstract

The two-dimensional (2D) graphyne-related scaffolds linked by carbon–carbon triple bonds have demonstrated promising applications in the field of catalysis and energy storage due to their unique features including high conductivity, permanent porosity, and electron-rich properties. However, the construction of related scaffolds was still mainly limited to the cross-linking of CaC_2 with multiple substituted aromatic halogens and there is still lack of efficient methodology capable of introducing high concentration heteroatoms within the architectures. Development of alternative and facile synthesis procedures to afford nitrogen-abundant graphyne materials is highly desirable yet challenging in the field of energy storage, particularly via the facile mechanochemical procedure under neat and ambient conditions. Herein, graphyne materials with abundant nitrogen-containing species (nitrogen content of 6.9–29.3 wt%), tunable surface areas (43–865 m^2 g^{-1}), and hieratical porosity were produced via the mechanochemistry-driven pathway by deploying highly electron-deficient multiple substituted aromatic nitriles as the precursors, which could undergo cross-linking reaction with CaC_2 to afford the desired nitrogen-doped graphyne scaffolds efficiently. Unique structural features of the as-synthesized materials contributed to promising performance in supercapacitor-related applications, delivering high capacitance of 254.5 F g^{-1} at 5 mV s^{-1}, attractive rate performance, and good long-term stability.

Keywords: graphyne, CaC$_2$, mechanochemistry, supercapacitor, energy storage

1. Introduction

The conjugated organic networks linked by alkynyl units, known as graphynes, have attracted extensive research efforts due to their unique features including rigid skeleton, porous architecture, π-conjugated structure, and abundant carbon–carbon triple bond within the scaffold.[1-5] Since the pioneering work of Li et al. in 2010, in which graphdiyne was synthesized via cross-coupling of hexaethynylbenzene precursors,[6] synthesis and application of graphyne-related materials have triggered broad interests in the field of catalysis and energy storage.[7-9] Notably, among diverse synthesis approaches towards graphyne construction, including but not limited to (1) on-surface coupling reactions on single crystal metal substrates under neat conditions;[10-11] (2) solution-based coupling reactions on solid–liquid or liquid–liquid interface;[6, 12] in which high vacuum and noble metals are required for pathway (1) and organic solvent, long reaction time (up to several days), high temperature, inert gas shielding are necessary for pathway (2). Comparatively, the mechanochemistry-driven methods (pathway (3)) could afford graphyne-related materials under neat and ambient conditions by leveraging the energy input from mechanochemical treatment to promote the nucleophilic attack reaction of CaC$_2$ with multiple substituted aromatic halides.[13-15] For example, mechanochemical treatment of CaC$_2$ and 1,2,4,5-tetrabromobenzene (TBB) mixture could produce graphyne materials via the nucleophilic attack of the electron-rich alkynyl anion on the C–Br bond in the TBB monomer.[16] Successive substitution of the C–Br bonds on the benzene ring by the alkynyl linkages afforded π-conjugated networks composed of abundant alkynyl moieties and benzene rings. Then the aromatic halide precursors were further extended to hexabromobenzene (HBB), 1,2,4,5-tetrachlorobenzene (TCB), halogenated hydrocarbon polymers, and aromatic rings.[16-19] However, the current mechanochemistry-driven methodology towards graphyne material construction was mainly limited to the aromatic halides or arene precursors, which could undergo cross-linking via the nucleophilic attack of the carbide on the C-X (X = H or halogen) bonds in the precursors. Although being recognized as a promising and widely used methodology in the construction of graphyne scaffolds, the current approaches were still lacking the capability to introduce high concentration of heteroatoms within the as-afforded graphyne scaffolds, which is critical to achieve enhanced performance in energy storage-related fields.

The development of electrochemical storage devices with improved efficiency and stability represents one of the most attractive strategies to solve the global potential energy crisis issue,[20-22] among which supercapacitors have gained considerable attention due to their rapid charge/discharge rate and high power density.[23-24] Notably, the π-conjugated structure, permanent porous property, and abundant defects within the networks of graphyne materials made them promising candidate as electrode materials in supercapacitor applications.[25] The graphyne materials derived from the mechanochemical treatment of CaC_2 and polyhalogenated hydrocarbons, possessing the surface area of 500–700 m^2 g^{-1}, displayed the supercapacitance of around 50–80 F g^{-1} at the current density of 1 A g^{-1}.[16] A highly preferable method of improving the capacitive performance of graphyne materials is via heteroatom doping (e.g., nitrogen-doping), which has been shown to enhance the capacitance of related materials by introducing pseudo capacitances and engineering wettability.[24, 26-27] In addition, significantly improved electrical conductivity was also achieved by nitrogen-doping within the material scaffolds, which could facilitate the formation of a localized electron-donor state near the Fermi level.[28] However, there are still limited approaches capable of affording abundant nitrogen moieties-involved graphyne materials. Post thermal treatment of graphyne derived from the crosslinking of CaC_2 with HBB in the presence of NH_4HCO_3 (as nitrogen source via decomposition) could introduce nitrogen species in the skeleton of graphyne, and the as-afforded materials performed well as electrodes in alkali-ion batteries.[29-30] Comparatively, approaches capable of producing abundant nitrogen-doped graphyne materials via direct cross-linking and in situ doping under mild conditions without tedious post-treatment and purification are more preferred. Initial efforts in this aspect included the utilization of tetrachloropyridine or cyanuric chloride as the nitrogen-containing monomers to construct nitrogen-doped graphyne via the cross-linking reaction with CaC_2.[13, 31] Although such progress has been made, state-of-the-art methods in the construction of nitrogen-doped graphyne materials are still limited to the active aromatic halides (monomers containing C–Cl bonds), with unsolved issues of relatively low nitrogen content in the as-afforded graphyne nanomaterials. Approaches capable of affording high-quality nitrogen-doped graphyne materials from unreactive aromatic halides (e.g., monomers containing C–F bonds) or alternative starting materials are still highly desired, particularly those that could deliver enhanced energy storage performance.

In this contribution, towards the construction of nitrogen-doped graphyne materials via the mechanochemistry-driven procedure under neat and mild conditions, multiple substituted aromatic halides with enhanced reactivity with CaC_2 were deployed by introducing extra electron-withdrawing cyano groups on the benzene ring, to achieve efficient graphyne scaffolds

construction and simultaneous nitrogen-doping. The as-afforded nitrogen-doped graphyne materials delivered enhanced energy storage behaviors in supercapacitor-related applications. Furthermore, the facile mechanochemical treatment pathway was extended to a non-halogenated monomer with multiple aromatic nitrile groups and electron-deficient properties, which could efficiently react with CaC_2 via the ball milling procedure. Efficient cross-coupling polymerization could be conducted with a low feeding mass ratio (CaC_2 : monomer) of 1:8 with almost quantitative yield. The as-afforded nitrogen-doped graphyne materials were featured by abundant nitrogen-containing species with nitrogen content in the range of 6.9–29.3 wt%, tunable surface areas in the range of 43–865 m^2 g^{-1}, and hierarchical architectures composed of micro- and mesopores, which could be regulated by varying the mechanochemical parameters. The unique properties of these materials worked together to deliver promising capacitance (up to 254.5 F g^{-1}) in supercapacitor-related applications, together with good rate performance and attractive cycling stability. The achievements made in this work not only provide monomers with highly conjugated structures coupled with high nitrogen content to construct task-specific graphyne materials but will also extend the application of related materials in other under-explored fields.
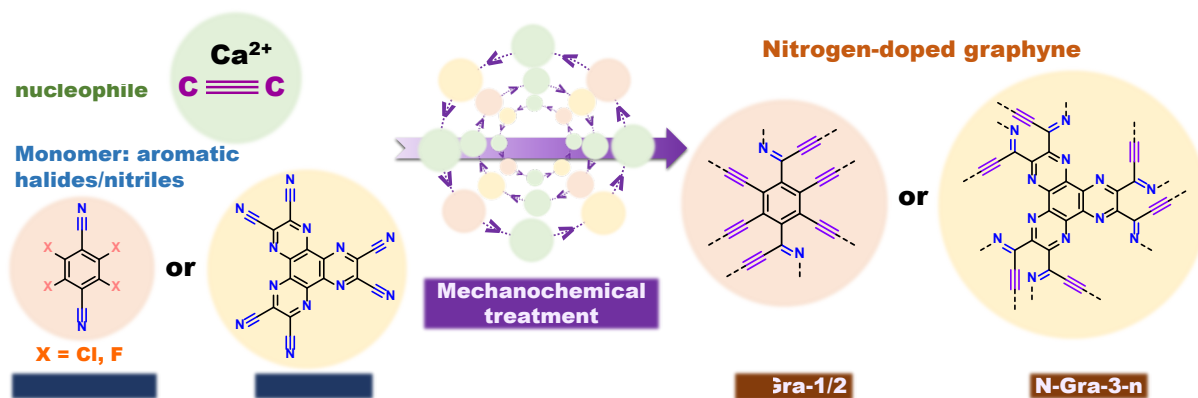

Figure 1. Schematic illustration of the nitrogen-doped graphyne materials construction via the mechanochemical treatment pathway using CaC_2 as the crosslinker and multiply-substituted aromatic halides or nitriles as the starting materials.

2 Results and Discussion

2.1 Synthesis, characterization, and supercapacitor performance of nitrogen-doped graphyne derived from TFTP and TCTP

Towards the construction of nitrogen-doped graphyne materials, the most straightforward way will be deploying monomers with nitrogen-containing functionalities in the structure, which

could react with CaC_2 promoted by mechanochemistry under neat and ambient conditions. Preliminary achievements on mechanochemical Ullmann-type reductive coupling of aromatic halides promoted by magnesium revealed that the reactivity of TCB could be significantly improved by introducing extra electron-withdrawing groups (e.g., -CN) on the benzene rings.[32] This envisaged us to explore the construction of nitrogen-doped graphyne materials using halogen- and cyano-group bi-functionalized monomers in which polymerization could be achieved by the nucleophilic attack of the carbide on multiple carbon–halogen bonds, and cyano groups could act as the nitrogen source. As an initial assessment, 2,3,5,6-tetrafluoroterephthalonitrile (TFTP) and 2,3,5,6-tetrachloroterephthalonitrile (TCTP) were deployed as starting materials to react with CaC_2 via mechanochemical treatment (Figure 1). For comparison, aromatic halides, including 1,2,4,5-tetrafluorobenzene (TFB), 1,2,4,5-tetrachlorobenzene (TCB), and 1,2,4,5-tetrabromobenzene (TBB), were used as the precursors to produce graphyne materials via the same ball milling procedure. The material synthesis was conducted with a mass feeding ratio (CaC_2 : monomer) of 1:1. The mixture was placed in a stainless-steel ball milling jar containing ball bearings and then treated by high-speed vibrating ball milling for 3 h. The product was collected after successively washing by diluted acid, water, and organic solvents to remove the unreacted starting materials, oligomers, and the as-formed metal species. After mechanochemical treatment for 3 h, no polymerized product was formed using TFB or TCB as the monomer, probably owing to the low activity of the C–F or C–Cl bonds in these two monomers to react with the carbide anions (Figure 2A). Comparatively, polymerization of TBB in the presence of CaC_2 afforded graphyne produce as black powder with the yield of 88.7% and the product was denoted as Gra-1. This was consistent with the reactivity of carbon–halogen bond in nucleophilic reaction (C–F < C–Cl < C–Br).[32] Notably, by introducing extra electron-withdrawing groups, herein as -CN groups, on the benzene rings, the reactivity of both TFTP and TCTP were significantly improved in CaC_2-promoted polymerization via mechanochemical treatment, affording nitrogen-doped graphyne materials, denoted as N-Gra-1 (yield: 83.7%) and N-Gra-2 (yield: 79.2%), respectively.

The textural properties of Gra-1 and N-Gra-1/2 obtained via the same mechanochemical treatment procedure was evaluated by N_2 adsorption/desorption isotherms collected at 77 K (Figure 2A–2B and S1–S2). The surface areas were calculated by the Brunauer-Emmett-Teller (BET) method, in which Gra-1 exhibited a surface area of 743 m^2 g^{-1}, and slightly diminished surface area of N-Gra-1 (229 m^2 g^{-1}) and N-GrA-2 (460 m^2 g^{-1}) were obtained (Figure S3–S4). Notably, the N_2 isotherms of these three materials displayed combined type I and type IV features, that is, rapid increase of the adsorption capacity at the low-pressure region ($P/P_0 < 0.1$)

together with a prominent hysteresis loop in the relatively high-pressure range, demonstrating their hierarchical porosity structures composed of micro- and mesopores. Pore size distribution curves obtained via the nonlocal density functional theory (NLDFT) method further demonstrated the co-existence of micropores (~1.5 nm) and mesopores (2-6 nm) in these graphyne materials being produced from the mechanochemical procedure (Figure 2C and S5). Detailed textural analysis revealed that the surface areas and pore volumes were mainly contributed by mesopores (Table S1). Specially, total pore volume of Gra-1, N-Gra-1, and N-Gra-2 was calculated to be 1.126, 0.269, 0.4 cm^3 g^{-1}, and the corresponding mesopore volume was 1.126, 0.263, 0.368 cm^3 g^{-1}, respectively. The architecture feature of Gra-1, N-Gra-1, and N-Gra-2 was characterized by the X-ray diffraction (XRD) patterns, with two peaks at $2\theta =$ 26.2° and 43.5° (Figure S6), indicating the graphitic structure of the as-afforded skeletons close to the graphite.[33-34] Graphitic morphology of the as-afforded scaffolds was further illustrated by (high resolution)-transmission electron microscopy ((HR)-TEM) images, which exhibited sheet-like architectures displaying a set of lattice fringes with a pacing of 0.34 nm and was consistent with the interplanar distance being calculated from the (002) diffraction peak at $2\theta =$ 26.2° (Figure S7 and S8). Successful introduction of nitrogen-doping in N-Gra-1/2 was verified by the elemental analysis, in which the nitrogen content of N-Gra-1 and N-Gra-2 was 6.28 wt% and 4.93 wt% (Figure 2A), respectively. Residual fluorine (0.35 wt% in N-Gra-1) and chlorine moieties (2.27 wt% in N-Gra-2) was also obtained by elemental analysis, demonstrating the possibility to produce halogen- and nitrogen-co-doped graphyne materials with enhanced performance in electrochemical applications (e.g., oxygen reduction reactions (ORR) and CO_2 reduction reactions (CO_2RR)).[35-36] The Raman spectrum of N-Gra-1 mainly displayed characteristic peaks for two-dimensional (2D) graphitic scaffolds in carbonaceous materials, including the G band at 1573.6 cm^{-1}, D band at 1342.2 cm^{-1}, and 2D band at 2673.3 cm^{-1}, and the I_D/I_G ratio of 1.06 was obtained using the Voigt function by fitting the spectrum (Figure 2D).

For materials in supercapacitor-related applications, the nitrogen-involved moieties could contribute pseudocapacitance in acidic media via Faradaic reactions: –C=NH + 2e +2H$^+$ = –CH–NH$_2$; –C–NHOH + 2e +2H$^+$ = –C–NH$_2$ + H$_2$O),[26] the conjugated scaffolds could promote the electron transfer, and the rigid porous channels could facilitate the fast ion diffusion during the charging/discharging process.[37] Therefore, the electrocapacitive performance of the obtained nitrogen-doped graphyne materials were investigated in 1 M H$_2$SO$_4$ electrolyte by cyclic voltammetry (CV) test, and compared with Gra-1 without nitrogen-doping. As shown in Figure 2E, 2F, and S9, N-Gra-1 and N-Gra-2 delivered a supercapacitance of 123.8 and 105.5 F g^{-1} at 5 mV s^{-1}, much higher than that obtained by using Gra-1 (69.7 F g^{-1}), although the

surface area of Gra-1 was higher than that of N-Gra-1/2 (Figure 2A). The results confirmed the critical role of nitrogen-doping towards enhanced supercapacitor performance and triggered us to explore alternative methods to produce graphyne materials with increased nitrogen content and improved porosity properties.
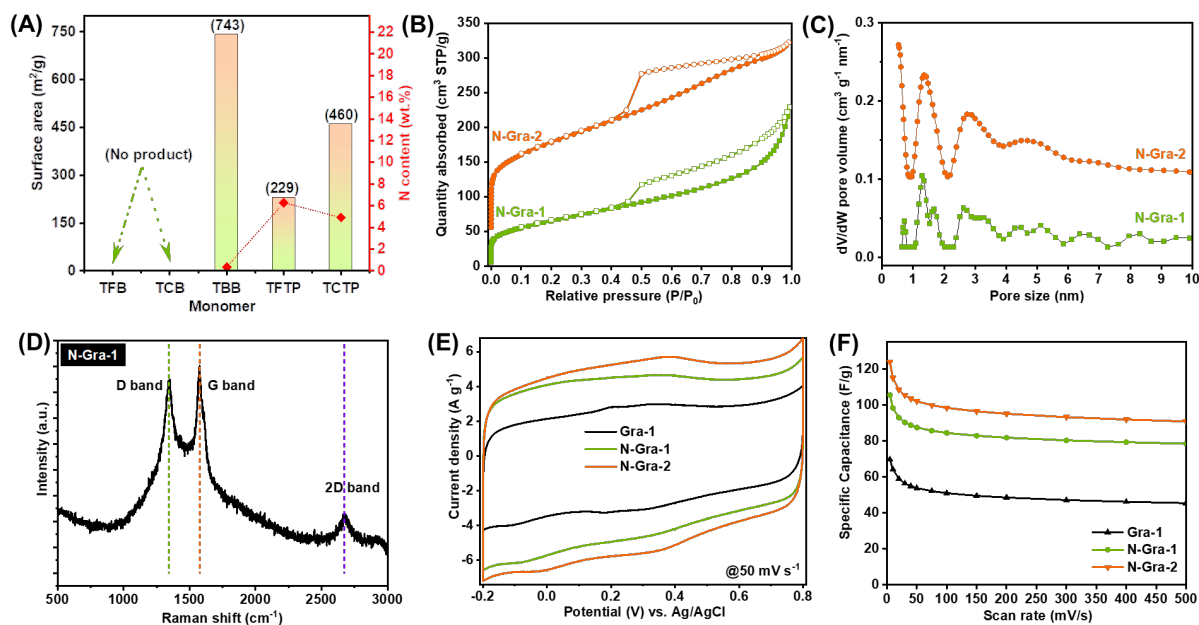

Figure 2. (A) BET surface area of Gra-1, N-Gra-1, and N-Gra-2 obtained from TBB, TFTP, and TCTP, respectively, together with the nitrogen content in the nitrogen-doped graphyne materials. (B) N_2 isotherms of N-Gra-1/2 collected at 77 K (values are offset along the y-axis by 50 cm^3 g^{-1} (orange). (C) Pore size distribution curve derived from NL-DFT method (values are offset along the y-axis by 0.1 cm^3 g^{-1} nm^{-1} (orange). (D) Raman spectrum of N-Gra-1. The supercapacitor performance of Gra-1 and N-Gra-1/2: (E) Cyclic voltammograms measured in 1 M H_2SO_4 at 50 mV s^{-1} with a Pt wire and Ag/AgCl electrode as counter electrode and reference electrode, respectively. (F) The specific capacitance calculated by integrating CV curves at different scan rates from 5 to 500 mV s^{-1}.

2.2 Synthesis, characterization, and supercapacitor performance of nitrogen-doped graphyne derived from HAT(CN)$_6$

Although N-Gra-1/2 displayed improved energy storage behavior compared with Gra-1 without nitrogen doping, the nitrogen content introduced by the cyano groups on the monomers was still not satisfactory. This envisaged us to explore the construction of nitrogen-doped graphyne materials using cyano group-abundant monomers without the involvement of carbon-halogen bond. To test the possibility, the electron-deficient and nitrogen-abundant aromatic nitrile

monomer 1,4,5,8,9,11-hexaazatriphenylenehexacarbonitrile [HAT(CN)$_6$] was deployed as the starting material to react with CaC$_2$ via mechanochemistry-driven procedure (Figure 1). With a ball milling time of 3 h, influence of CaC$_2$ feeding amount on the BET surface area of the as-afforded nitrogen-doped graphyne materials was studied, and the products were denoted as N-Gra-3-n (n = mass ratio of CaC$_2$: HAT(CN)$_6$ being added) (Figure 3A and S10-S15). Even with low mass ratio (CaC$_2$: HAT(CN)$_6$) of 0.125, polymerized product N-Gra-3-0.125 was obtained with high yield (91.4%), indicating the high reactivity of HAT(CN)$_6$ with CaC$_2$ via nucleophilic attack procedure. However, the surface area of the graphyne materials obtained by adding CaC$_2$ with the mass ratio (CaC$_2$: HAT(CN)$_6$) less than 1 was relatively low (43-54 m^2 g^{-1}). Comparatively, surface area of the as-formed materials gradually increased to 313 (N-Gra-3-1.5), 523 (N-Gra-3-2) and 865 m^2 g^{-1} (N-Gra-3-3), probably owing to the improved polymerization degree in the presence of more catalyst/crosslinker. While further increasing the mass ratio (CaC$_2$: HAT(CN)$_6$) to 4 led to diminished surface area of N-Gra-3-4 (92 m^2 g^{-1}) caused by the monomer [HAT(CN)$_6$] dilution effect. The coupling polymerization was driven by the mechanical forces between the ball bears and reactants, while too much CaC$_2$ would reduce the interaction chance of HAT(CN)$_6$ with CaC$_2$, leading to the deficient polymerization. In addition, the ball milling reaction time could also affect the surface area of the as-formed materials with a feeding mass ratio (CaC$_2$: HAT(CN)$_6$) of 2, for which the surface area of N-Gra-3-2 gradually increased from 170, 523, to 687 m^2 g^{-1} with the ball milling time varying from 1 h to 3 h to 5 h. This may influence the supercapacitor performance of the as-produced graphyne materials. The N$_2$ isotherm of N-Gra-3-1 displayed type I shape, indicating the microporous structure with pore size distribution around 0.64 nm (Figure 3B and 3C). Comparatively, N$_2$ isotherms of the materials N-Gra-3-n (n = 1.5, 2, and 3) obtained by adding more CaC$_2$ exhibited combined features of type I and type IV, similar to the porosity structure of N-Gra-1/2, and the pore size distribution curves obtained from the NLDFT method demonstrated the existence of micropore around 1.2 nm and mesopore around 2.5 nm. The porosity parameters of the N-Gra-3-n materials were summarized in Table S2. It should be noted that the pore structure played a crucial role in determining the capacitive performance for porous materials.[38] Small micropore (less than 1 nm) could contribute a high charge storage capability under low current density due to closer approach of the highly distorted solvation ion center to the electrode surface, but they also posed difficulties for the diffusion and transfer of electrolyte ions, resulting in the poor rate capacitance.[39-40] Contrarily, the pores larger than 5 nm could achieve fast electrolyte transportation but only contribute low charge storage. Therefore, porous materials with large micropores in the range of 1–2 nm coupled with

mesopores in the range of 2–5 nm, like N-Gra-3-n (n = 1.5, 2, and 3), were preferred to harvest higher specific capacitances and faster charge propagation simultaneously in supercapacitor-related applications.[41-42] The nitrogen content of the N-Gra-3 materials from different mechanochemical conditions measured by elemental analyis revealed that nitrogen content up to 29.3 wt% was obtained in N-Gra-3-0.25 (Figure 3D). By adding more CaC_2 in the starting material (n = 0.5 to 3.0), although surface area of the as-afforded graphyne materials was increased due to higher polymerization degree, the nitrogen content varied from 26.71 wt% to 6.90 wt% probably owing the introduction of more carbon-carbon triple bond within the scaffolds. Notably, different nitrogen contents and porosity properties of the nitrogen-doped graphyne materials could deliver varied energy storage behavior as supercapacitors. The N-Gra-3-n derived from various mechanochemical treatment conditions were amorphous, as indicated by the PXRD patterns, with no extra peaks for the presence of impurities (Figure S16). Raman spectrum of N-Gra-3-2 displayed the characteristic peaks of G band (1541.67 cm^{-1}), D band (1352.31 cm^{-1}), and broad 2D band (2840.97 cm^{-1}), with the I_D/I_G ratio of 1.15 (Figure 3E). The presence of large amounts of unpaired spins within the skeleton of N-Gra-3-2 derived from the nitrogen-containing species and the electron-rich carbon–carbon triple bonds was revealed by the electron paramagnetic resonance (EPR) spectrum with a predominant peak centered at 3452 G and a *g* value of 2.004 (Figure 3F). The asymmetric shape of the peak indicated that the unpaired spins existed both within the skeleton and at the edge positions.[43] The chemical bonding information of N-Gra-3-2 was further investigated by X-ray photoelectron spectroscopy (XPS) analysis (Figure 3G and 3H). In the C1s XPS spectrum, it could be deconvoluted to four peaks corresponding to the aromatic carbon with the fused rings with binding energy (BE) of 284.2 eV, carbon signals derived from the carbide anion (BE = 285.0 eV), carbon atoms being connected to the nitrogen atoms in the form of C=N bonds (BE = 286.04 eV), and those connected to nitrogen species with positive charge being formed during the acid washing procedure (BE = 287.98 eV).[29] Correspondingly, in the N1s spectrum, four types of nitrogen-containing species, including the pyridinic nitrogen (BE = 398.6 eV), pyrrolic nitrogen (399.9 eV), quaternary nitrogen with positive charge (BE = 400.8 eV), and a small amount of oxidized nitrogen counterparts (BE = 402.5 eV).[44-45] As shown in Figure S17, the band at around 1622 and 1402 cm^{-1} of Fourier-transform infrared (FTIR) spectrum corresponds to the vibration of aromatic rings and C=N. The band at around 1086 cm^{-1} was assigned to the asymmetric stretching of C–C which is beside the C≡C as shown in Figure 1. The signal for C≡C appeared at around 2213 cm^{-1} for N-Gra-3. Owing to the extensively conjugated architecture of N-Gra-3-2, the solid-state ^{13}C nuclear magnetic resonance (^{13}C NMR) collected

by the direct polarization magic-angle spinning (DPMAS) experiment only exhibited a broad peak in the range of 70–200 ppm, including the carbon-carbon triple bonds, aromatic carbon signals, and the moieties including C–N bonds formation (Figure 3I). The morphology characterization of N-Gra-3-2 revealed that the materials was composed of bulk particles with sheet-like structures at the edge sites, as shown in the scanning electron microscopy (SEM) and TEM images (Figure 3J and 3K). The thickness of the chunks was in the range of 359 nm-1.7 μm, as indicated by the atomic force microscopy (AFM) results (Figure S18). The elemental mapping (Figure S19) shows the uniform distribution of C, N elements.
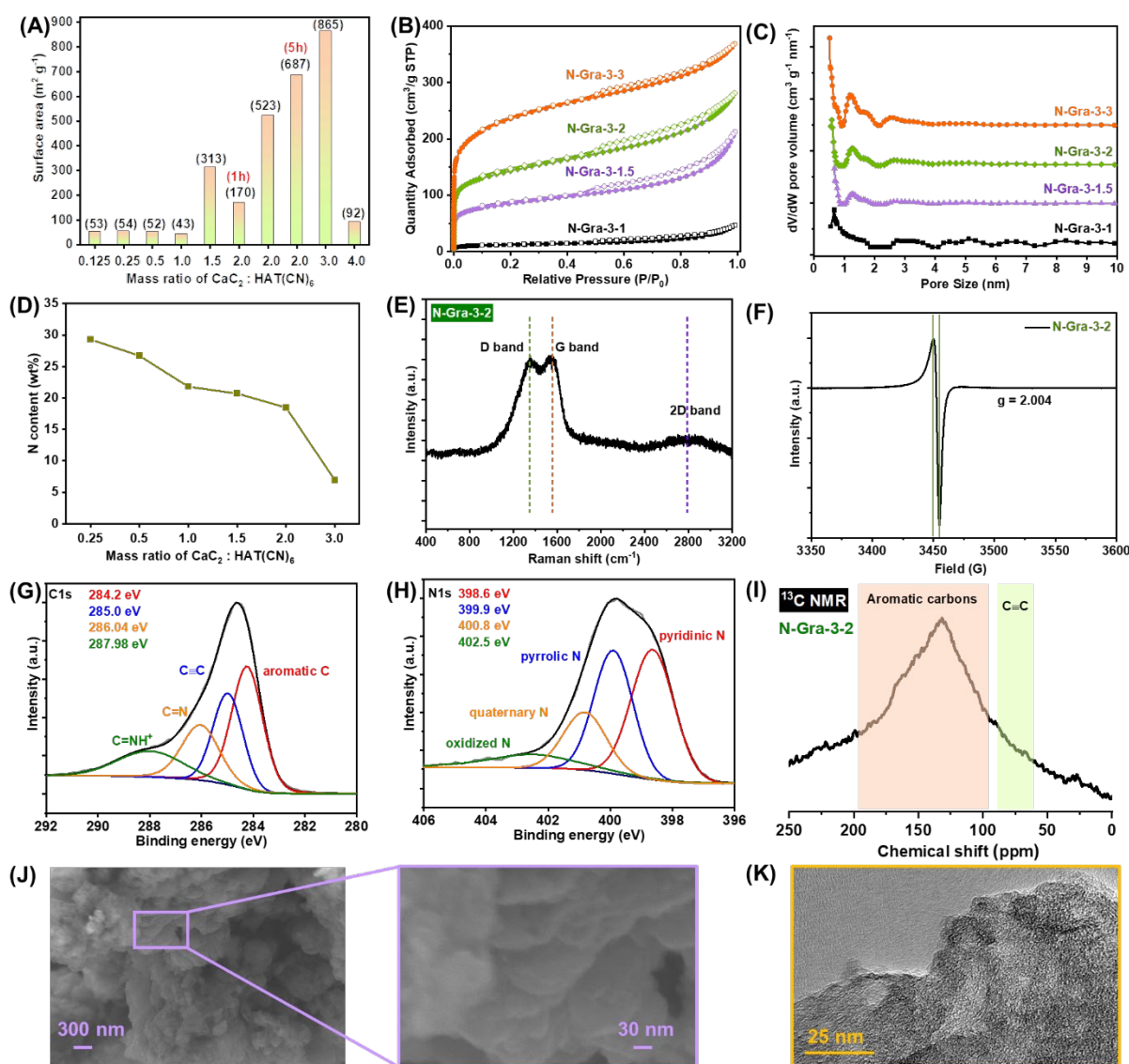

Figure 3. (A) BET surface areas of nitrogen-doped graphyne derived from $HAT(CN)_6$ (N-Gra-3-n) afforded by ball milling with different CaC_2 loading and ball milling time. (B) N_2 isotherms of N-Gra-3-1.0/1.5/2.0/3.0 collected at 77 K. (C) Pore size distribution curve derived from NL-DFT method of N-Gra-3-1.0/1.5/2.0/3.0. (D) the nitrogen content in the N-Gra-3-n. Detailed characterizations for N-Gra-3-2.0: (E) Raman spectrum of N-Gra-3-2. (F) EPR spectrum. (G)

XPS spectrum for C 1s. (H) XPS spectrum for N 1s. (I) DNP-CP/MAS ^{13}C NMR spectrum. (J) SEM images. (K) TEM images.

Considering the abundant nitrogen-containing species, high surface areas, and hierarchical porous structure of the as-produced nitrogen-doped graphyne materials using HAT(CN)$_6$ as the starting material, their performance as electrode materials in supercapacitor-related application was then studied. CV curves of the N-Gra-3-n derived from different feeding mass ratio of CaC$_2$: HAT(CN)$_6$ were collected using 1 M H$_2$SO$_4$ as the electrolyte with the scan rate ranging from 5 to 500 mV s^{-1} (Figure 4A, 4B, and S20). Generally, for N-Gra-3-n (n = 0.25, 0.5, and 4) possessing low surface areas (43–92 m^2 g^{-1}) and pore volumes (less than 0.1 cm^3 g^{-1}), the as-calculated capacitance was quite low (< 80 F g^{-1}) despite the high nitrogen content in these materials, probably caused by the low diffusion rate of the electrolyte ions and the low electronic conductivity of the scaffolds derived from the low polymerization degree. Their capacitance mainly originated from the pseudo-capacitance involving the redox reactions of nitrogen-containing moieties, as authenticated by the CV shapes, which were not quasi-rectangle. A significantly improved performance at low scan rate was observed in N-Gra-3-n (n = 1, 1.5, 2) with higher surface areas (up to 523 m^2 g^{-1}) and moderate nitrogen content (18.46-21.79 wt%), delivering the capacitance of 190.7–254.5 F g^{-1} with the scan rate of 5 mV s^{-1}. However, their rate performance at high scan rates was still not satisfied (< 45% capacitance retention at 500 mV s^{-1}), indicating that optimized pore structures were still required to achieve fast charging/discharging.[46] Indeed, N-Gra-3-3 with further enhanced surface area (865 m^2 g^{-1}) displayed promising capacitance retention at high scan rates, with the capacitance of 124.0 F g^{-1} being obtained at 500 mV s^{-1}, corresponding to 67.0 % retention of the capacitance at 5 mV s^{-1}. Notably, the supercapacitor performance of the HAT(CN)$_6$-derived nitrogen-doped graphyne materials via mechanochemistry surpassed that being achieved by the non-heteroatom-doped graphyne scaffolds and was among the best ones compared with the heteroatom-doped carbon materials (Table S4).

As previously reported, the benefits of nitrogen-doping in electrochemical property improvement lie in the enhanced surface wettability of the porous scaffolds, which could favor the effective ion-accessible surfaces and bring enhanced contribution to capacitance, particularly when aqueous electrolytes were adopted.[47] In addition, the nitrogen-involved species could contribute pseudocapacitance in acidic media.[26] In order to gain further insight into the pseudocapacitance derived from the abundant N content and the capacitive capacitance from the electric double layer capacitor (EDLC) in the afforded N-Gra-3 structures, kinetical

features were studied based on the recorded CV data. It should be noted that the current density of the supercapacitor is related with the scan rate (v), based on the equation of $i = a*v^b$, where $b = 1$ represents the ideal capacitive behavior, $b = 0.5$ represents a diffusion controlled kinetic process, and $b = 0.5$-1 represents an amalgam of diffusion and capacitive processes. The b value could be obtained by plotting the logarithm of the current densities against the logarithm of scan rates ($\log i = a + b \log v$).[48] In Figure 4C, it was shown that the b values of N-Gra-3-0.5, N-Gra-3-1.0, N-Gra-3-2.0, and N-Gra-3-3.0 were 0.652, 0.802, 0.913, and 0.946 respectively, and the higher the CaC_2 amount being added during the ball milling process, the higher the b value, indicating a greater capacitive contribution to the capacitance. To further demonstrate this, the Dunn method based on the $i = k_1 v + k_2 v^{0.5}$ equation was used to quantitatively analyze the contribution of the capacitive capacitance and the diffusion-controlled capacitance.[49] As shown in Figure S22, the supercapacitance of N-Gra-3-0.5 were dominated by the diffusion-controlled process (89.7% at 5 mV s^{-1}), which was consistent with the non-rectangular shape of the CV curves. With the increasing amount of CaC_2 from N-Gra-3-0.5 to N-Gra-3-3, the capacitive contribution increased from 10.3% to 67.5% at 5 mV s^{-1}, which was due to the increased surface area and decreased N content. Additionally, the capacitive contribution increased with scan rate, while the pseudocapacitance decreased, consistent with the fact that pseudocapacitance was controlled by the diffusion process, especially at high scan rates. In addition, extending the ball milling period could also enhance the rate performance of the obtained N-Gra-3-2 materials (Figure 4D, 4E, and S21). For example, N-Gra-3-2-5 h achieved a capacitance of 195.7, 184.3, 173.8, 161.2, 153.2, 145.0 and 132.7 F g^{-1} at scan rate of 5, 10, 20, 50, 100, 200, and 500 mV s^{-1}, respectively. Comparatively, although N-Gra-3-2-3 h possessed a higher capacitance at a low scan rate, the rate performance was inferior. While N-Gra-3-2-1 h with low polymerization degree and surface area delivered diminished capacitance regardless of the scan rates, which is consistent with the kinetics study as shown in Figure 4F and Figure S22, the longer the ball milling time, the more capacitive contribution and thus better rate capacities. To better understand the charge/discharge properties of the N-Gra-3, galvanostatic charge–discharge (GCD) curves of N-Gra-3-2-5 h from the current density of 1 to 100 A g^{-1} were collected, which exhibited a triangle distribution, indicating superior capacitive behaviors (Figure 4G). A high capacitance of 203.4 F g^{-1} at a current density of 1 A g^{-1} was obtained, which was comparable to the result obtained from CV curves at 5 mV s^{-1} (equivalent to a current density of approximately 1.05 A g^{-1}). Moreover, the N-Gra-3-2-5 h maintained a high capacity of 120 F g^{-1} under the much higher current density of 100 A g^{-1}, which demonstrated a rapid and efficient charge transfer rate due to the abundant pore structures

as well as the π-conjugated skeletons (Figure 4H). Moreover, N-Gra-3-2-5 h displayed excellent cycling stability with a 90% retention in capacitance after 6000 cycles at 5 A g^{-1} (Figure 4I). The SEM images of N-Gra-3-2-5 h before and after long cycling shows similar sheet-like morphology, indicating good structure stability (Figure S23). Beyond that, the counterpart of HAT(CN)$_6$, namely 2,3,6,7,10,11-hexabromotriphenylene (HBTP) with a similar π-conjugated macromolecular structure (as shown in Figure S24) was also ball milled with CaC$_2$ and afforded graphyne material (denoted as Gra-2) and then was explored as electrode material for supercapacitor (Figure S25). Gra-2 exhibited a capacitance of 139.3 F g^{-1} at the scan rate of 5 mV s^{-1} and retained 84.6 F g^{-1} at 500 mV s^{-1}. Although the results were better than the Gra-1, still inferior compared with N-Gra-3 with equivalent surface area (818.6 m^2 g^{-1}, Figure S26), indicating the importance of highly conjugated monomer and high nitrogen content in the mechanochemical method derived graphyne materials for electrochemical fields.
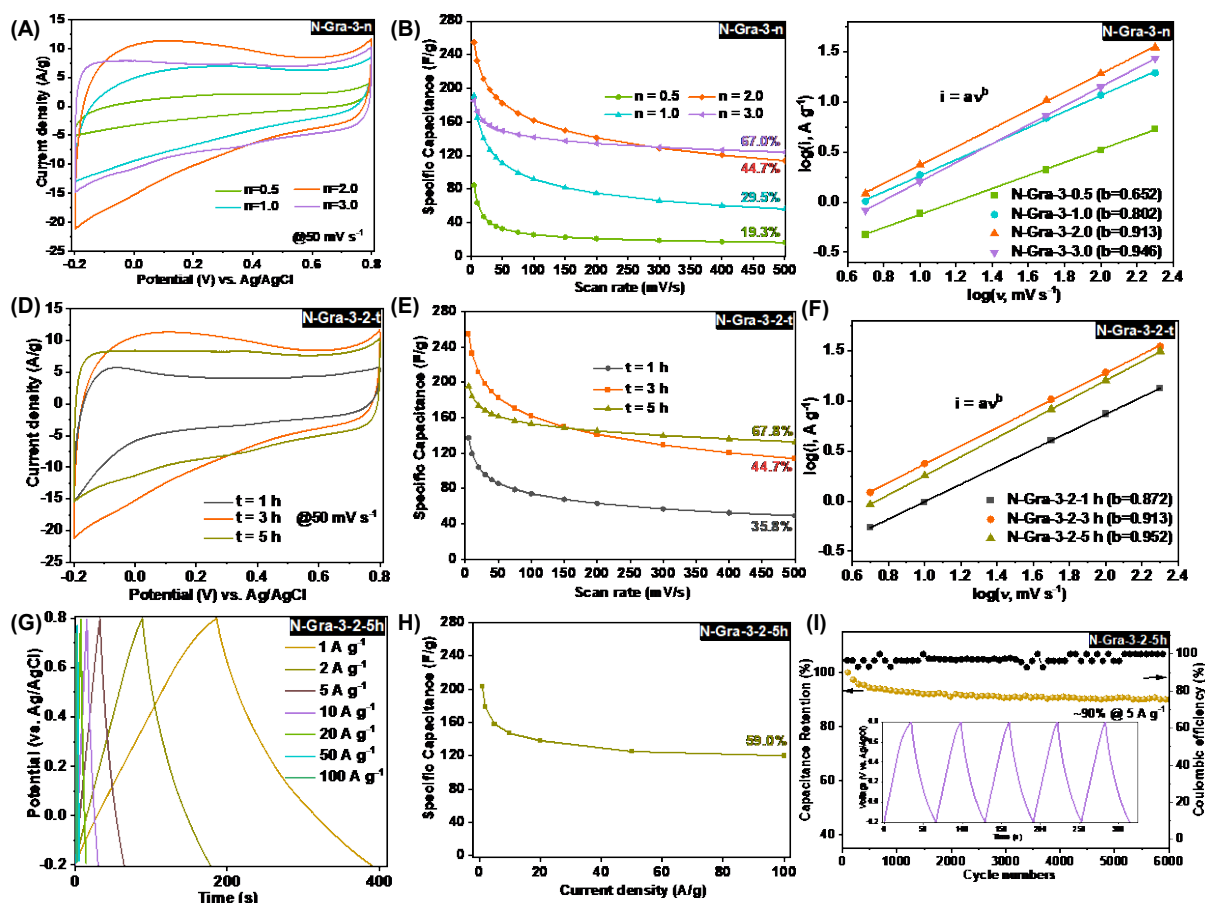

Figure 4. Electrochemical performance of N-Gra-3-n: (A) Typical CV curves measured at the scan rate of 50 mV s^{-1}. (B) The specific capacitance calculated by integrating CV curves at different scan rates from 5 to 500 mV s^{-1}. (C) Log (i) vs log (v) and the fitting line based on the CV curves of 5, 10, 50, 100, 200 mV s^{-1}. Electrochemical performance of N-Gra-3-2 afforded with different ball milling time: (D) Typical CV curves measured at the scan rate of 50 mV s^{-1}.

13

(E) The specific capacitance calculated by integrating CV curves at different scan rates from 5 to 500 mV s^{-1}. (F) Log (i) vs log (v) and the fitting line based on the CV curves of 5, 10, 50, 100, 200 mV s^{-1}. N-Gra-3-2 (5 h): (G) GCD curves from the current density of 1 to 100 A g^{-1}. (H) Supercapacitance calculated by the GCD results. (I) Supercapacitance retention and coulombic efficiency calculated by GCD curves at 5 A g^{-1} and the insert is the first 5 cycles of GCD curves.

To further demonstrate its electrochemical performance, the obtained N-Gra-3 was tested in a symmetric two-electrode supercapacitor system with 1 M Na$_2$SO$_4$ as electrolyte. Neutral Na$_2$SO$_4$ electrolyte will achieve a higher energy density due to its wide operating voltage of 1.8 V. Take N-Gra-3-2-5 h as a representative, CV curves as shown in Figure 5A exhibited the quasi-rectangular shapes even at the high scan rate of 100 mV s^{-1}, demonstrating excellent rate ability of the N-Gra-3 electrodes. Additionally, the GCD curves (Figure 5B) at various current densities displayed linear and symmetrical triangular shapes, confirming excellent electrochemical capacitive behavior, which was consistent with the results in Figure S22. The specific capacitances calculated from the GCD curves (Figure 5C) showed the specific capacitance of 88 and 39 F g^{-1} at 0.2 and 10 A g^{-1}, respectively. To better understand the reason underlying the excellent performance, electrochemical impedance spectroscopy (EIS) was also conducted. In Figure 5D, a nearly vertical line can be seen in the low-frequency region, confirming its excellent capacitive behavior. Moreover, there was a combination of electrode interfacial resistance and electrolyte ionic resistance as low as 2.25 Ω, indicating superior electron conductivity and rapid ion exchange between the electrode and electrolyte. Furthermore, the assembled symmetric supercapacitor exhibits a competitive energy density of 10 Wh kg^{-1} at a corresponding power density of 90 W kg^{-1}, and 7.7 Wh kg^{-1} at 0.9 kW kg^{-1} (Figure 5E), which was comparable with that being obtained by the previously reported carbon symmetric supercapacitors in aqueous electrolyte, such as ordered mesoporous carbons (4−6 Wh kg^{-1} at 0.8−1.05 kW kg^{-1}),[50] nitrogen-doped porous carbon (11.9 Wh kg^{-1} at 0.46 kW kg^{-1}).[51]
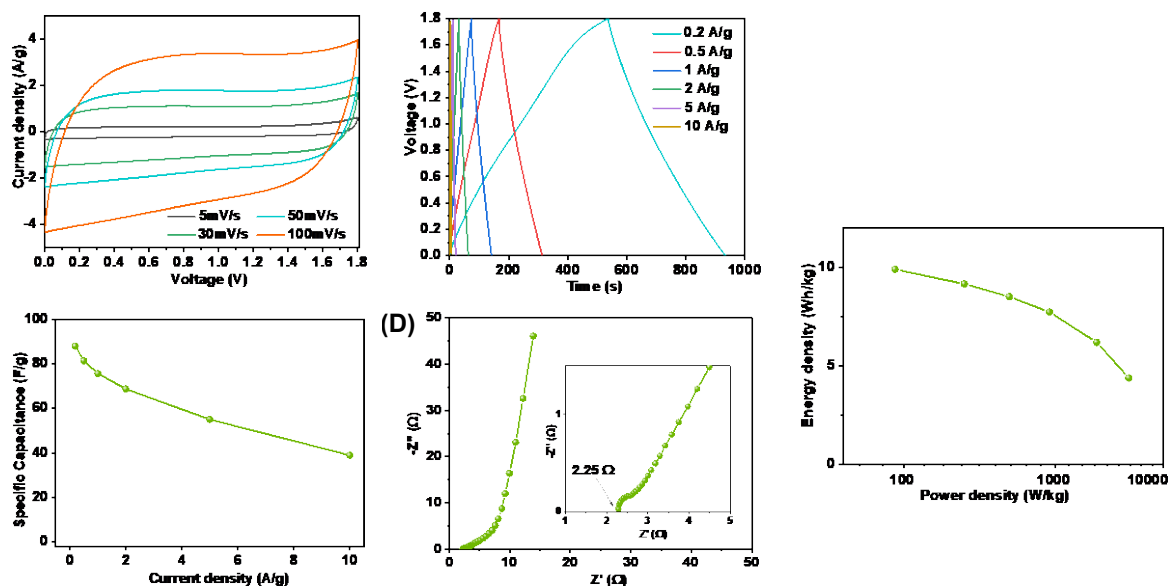
Figure 5. Electrochemical performance of symmetric supercapacitor of N-Gra-3-2-5 h with 1 M Na$_2$SO$_4$ as electrolyte. (A) CV curves at different scan rates. (B) GCD curves at various current densities. (C) the specific capacitance derived from GCD curves. (D) EIS Nyquist plots; (E) Ragone plot (energy density vs. power density).

3 Conclusion

Considering the advantages of introducing extra nitrogen-containing species into the graphyne scaffolds towards enhanced performance in energy storage, a facile mechanochemistry-driven pathway was developed by leveraging the chemical structures of the monomers. Initial study by deploying multiple substituted aromatic halogens with extra nitrile groups on the benzene ring demonstrated the high reactivity of these monomer with CaC$_2$ via the ball milling procedure, which could afford nitrogen-doped graphyne materials with the involvement of the cyano groups in the polymerization process. An alternative electron-deficient aromatic nitrile monomer was then deployed to construct graphyne scaffolds with abundant nitrogen-containing species, high surface areas, and permanent porosities. Unique properties of the as-afforded materials provided them with attractive performance in energy storage applications. The synthesis approaches developed in this work could produce nitrogen-doped graphyne scaffold with controllable properties and will further extend the application of these materials in alternative fields.

Acknowledgements

Conflict of Interest

The authors declare no conflict of interest.

Supporting Information

Supporting Information is available from the Wiley Online Library or from the author.

[1]   Q. Pan, S. Chen, C. Wu, F. Shao, J. Sun, L. Sun, Z. Zhang, Y. Man, Z. Li, L. He, Y. Zhao, *CCS Chem.* **2020**, *3*, 1368-1375.
[2]   Y. Li, S. Li, X. Xu, H. Meng, Y. Lu, C. Li, *Green Energy Environ.* **2021**, *in press, DOI: 10.1016/j.gee.2021.04.007*.
[3]   Y. Li, S. Li, X. Xu, J. Gu, X. He, H. Meng, Y. Lu, C. Li, *ACS Sustain. Chem. Eng.* **2021**, *9*, 9221-9229.
[4]   X. Li, N. Wang, J. He, Z. Yang, Z. Tu, F. Zhao, K. Wang, Y. Yi, C. Huang, *Carbon* **2020**, *162*, 579-585.
[5]   R. R. Tykwinski, *Angew. Chem. Int. Ed.* **2003**, *42*, 1566-1568.
[6]   G. Li, Y. Li, H. Liu, Y. Guo, Y. Li, D. Zhu, *Chem. Commun.* **2010**, *46*, 3256-3258.
[7]   Y. Gong, L. Shen, Z. Kang, K. Liu, Q. Du, D. Ye, H. Zhao, X. A. Sun, J. Zhang, *J. Mater. Chem. A* **2020**, *8*, 21408-21433.
[8]   X. Li, H. Zhang, L. Chi, *Adv. Mater.* **2019**, *31*, 1804087.
[9]   Y. Li, L. Xu, H. Liu, Y. Li, *Chem. Soc. Rev.* **2014**, *43*, 2572-2586.
[10]   H.-Y. Gao, H. Wagner, D. Zhong, J.-H. Franke, A. Studer, H. Fuchs, *Angew. Chem. Int. Ed.* **2013**, *52*, 4024-4028.
[11]   X. Li, H. Zhang, L. Chi, *Adv. Mater.* **2019**, *31*, e1804087.
[12]   Y. Song, X. Li, Z. Yang, J. Wang, C. Liu, C. Xie, H. Wang, C. Huang, *Chem. Commun.* **2019**, *55*, 6571-6574.
[13]   Y. Chen, Q. D. Li, W. J. Wang, Y. X. Lu, C. L. He, D. Qiu, X. L. Cui, *2D Mater.* **2021**, *8*, 044012.
[14]   Y. Li, Y. Li, X. He, J. Gu, M. Yu, W. Li, C. Li, *SN Appl. Sci.* **2019**, *1*, 195.
[15]   S. L. James, C. J. Adams, C. Bolm, D. Braga, P. Collier, T. Friščić, F. Grepioni, K. D. M. Harris, G. Hyett, W. Jones, A. Krebs, J. Mack, L. Maini, A. G. Orpen, I. P. Parkin, W. C. Shearouse, J. W. Steed, D. C. Waddell, *Chem. Soc. Rev.* **2012**, *41*, 413-447.
[16]   Y. Li, Q. Liu, W. Li, H. Meng, Y. Lu, C. Li, *ACS Appl. Mater. Interfaces* **2017**, *9*, 3895-3901.
[17]   C. Yang, Y. Li, Y. Chen, Q. Li, L. Wu, X. Cui, *Small* **2019**, *15*, 1804710.
[18]   X. Xu, Y. Lu, H. Meng, C. Li, *Chem. Eng. J.* **2019**, *372*, 181-190.

[19] Q. Liu, L. Cheng, X. Xu, H. Meng, Y. Lu, C. Li, *Chem. Eng. Process.* **2018**, *124*, 261-268.

[20] S. Chen, K. Wen, J. Fan, Y. Bando, D. Golberg, *J. Mater. Chem. A* **2018**, *6*, 11631-11663.

[21] Z. Yang, T. Wang, H. Chen, X. Suo, P. Halstenberg, H. Lyu, W. Jiang, S. M. Mahurin, I. Popovs, S. Dai, *ACS Energy Lett.* **2021**, *6*, 41-51.

[22] H. Chen, X. Suo, Z. Yang, S. Dai, *Adv. Mater.* **2022**, *34*, 2107947.

[23] B. K. Saikia, S. M. Benoy, M. Bora, J. Tamuly, M. Pandey, D. Bhattacharya, *Fuel* **2020**, *282*, 118796.

[24] J. Fan, T. Wang, H. Chen, Z. Wang, B. P. Thapaliya, T. Kobayashi, Y. Yuan, I. Popovs, Z. Yang, S. Dai, *Adv. Funct. Mater.* **2022**, *32*, 2202669.

[25] Y. Xu, R. S. Sprick, N. J. Brownbill, F. Blanc, Q. Li, J. W. Ward, S. Ren, A. Cooper, *J. Mater. Chem. A* **2021**, *9*, 3303-3308.

[26] S. L. Candelaria, B. B. Garcia, D. W. Liu, G. Z. Cao, *J. Mater. Chem.* **2012**, *22*, 9884-9889.

[27] L. Zhao, L. Z. Fan, M. Q. Zhou, H. Guan, S. Qiao, M. Antonietti, M. M. Titirici, *Adv. Mater.* **2010**, *22*, 5202-5206.

[28] S. Zhang, S. Tsuzuki, K. Ueno, K. Dokko, M. Watanabe, *Angew. Chem. Int. Ed.* **2015**, *54*, 1302-1306.

[29] C. Yang, C. Qiao, Y. Chen, X. Zhao, L. Wu, Y. Li, Y. Jia, S. Wang, X. Cui, *Small* **2020**, *16*, 1907365.

[30] W. J. Lee, J. Lim, S. O. Kim, *Small Methods* **2017**, *1*, 1600014.

[31] M. E. Casco, S. Kirchhoff, D. Leistenschneider, M. Rauche, E. Brunner, L. Borchardt, *Nanoscale* **2019**, *11*, 4712-4718.

[32] H. Chen, J. Fan, Y. Fu, C.-L. Do-Thanh, X. Suo, T. Wang, I. Popovs, D. Jiang, Y. Yuan, Z. Yang, S. Dai, *Adv. Mater.* **2021**, *33*, 2008685.

[33] M. D. Hossain, Q. Zhang, T. Cheng, W. A. Goddard, Z. Luo, *Carbon* **2021**, *183*, 940-947.

[34] Y. T. Yuan, T. Wang, H. Chen, S. M. Mahurin, H. M. Luo, G. M. Veith, Z. Z. Yang, S. Dai, *Angew. Chem. Int. Ed.* **2020**, *59*, 21935-21939.

[35] T. Gong, R. Qi, X. Liu, H. Li, Y. Zhang, *Nano-Micro Lett.* **2019**, *11*, 1-11.

[36] D. Xue, H. Xia, W. Yan, J. Zhang, S. Mu, *Nano-Micro Lett.* **2021**, *13*, 1-23.

[37] Z. Zhang, M. Liao, H. Lou, Y. Hu, X. Sun, H. Peng, *Adv. Mater.* **2018**, *30*, 1704261.

[38] J. Hou, K. Jiang, M. Tahir, X. Wu, F. Idrees, M. Shen, C. Cao, *J. Power Sources* **2017**, *371*, 148-155.

[39] Y. Li, D. Zhang, Y. Zhang, J. He, Y. Wang, K. Wang, Y. Xu, H. Li, Y. Wang, *J. Power Sources* **2020**, *448*, 227396.

[40] J. Chmiola, G. Yushin, Y. Gogotsi, C. Portet, P. Simon, P. L. Taberna, *Science* **2006**, *313*, 1760-1763.

[41] J. Huang, B. G. Sumpter, V. Meunier, *Chem. Eur. J.* **2008**, *14*, 6614-6626.

[42] K. Kraiwattanawong, *Arabian J. Chem.* **2022**, *15*, 103625.

[43] A. Barbon, M. Brustolon, *Appl. Magn. Reson.* **2012**, *42*, 197-210.

[44] L. Roldán, S. Armenise, Y. Marco, E. García-Bordejé, *Phys. Chem. Chem. Phys.* **2012**, *14*, 3568-3575.

[45] X. Chen, Q. Xu, B. Zhao, S. Ren, Z. Wu, J. Wu, Y. Yue, D. Han, R. Li, *Catal. Lett.* **2021**, *151*, 3372-3380.

[46] Y. Li, S. Zheng, X. Liu, P. Li, L. Sun, R. Yang, S. Wang, Z.-S. Wu, X. Bao, W.-Q. Deng, *Angew. Chem. Int. Ed.* **2018**, *57*, 7992-7996.

[47] W. Zhang, C. Xu, C. Ma, G. Li, Y. Wang, K. Zhang, F. Li, C. Liu, H.-M. Cheng, Y. Du, N. Tang, W. Ren, *Adv. Mater.* **2017**, *29*, 1701677.

[48] B. Yao, S. Chandrasekaran, H. Zhang, A. Ma, J. Kang, L. Zhang, X. Lu, F. Qian, C. Zhu, E. B. Duoss, C. M. Spadaccini, M. A. Worsley, Y. Li, *Adv. Mater.* **2020**, *32*, 1906652.

[49] J. Wang, J. Polleux, J. Lim, B. Dunn, *J. Phys. Chem. C* **2007**, *111*, 14925-14931.

[50] W. Xing, S. Z. Qiao, R. G. Ding, F. Li, G. Q. Lu, Z. F. Yan, H. M. Cheng, *Carbon* **2006**, *44*, 216-224.

[51] L. Guan, L. Pan, T. Peng, C. Gao, W. Zhao, Z. Yang, H. Hu, M. Wu, *ACS Sustain. Chem. Eng.* **2019**, *7*, 8405-8412.

Mechanochemical Construction of Nitrogen-abundant Graphyne Scaffolds with Enhanced Performance as Supercapacitors

Juntian Fan, Tao Wang, Bishnu P. Thapaliya, Meijia Li, Chi-Linh Do-Thanh, Takeshi Kobayashi, Ilja Popovs, Zhenzhen Yang*, and Sheng Dai*
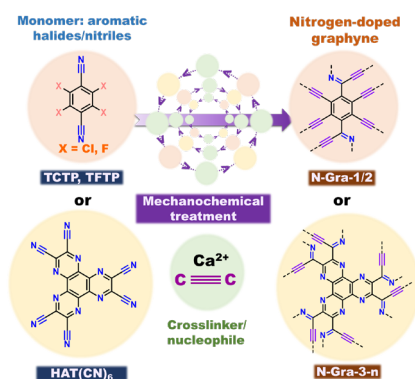
Graphyne materials with abundant nitrogen-containing species (nitrogen content up to 29.31 wt%), high surface areas, and hieratical porosity were produced via the mechanochemistry-driven pathway by deploying highly electron-deficient multiple substituted aromatic nitriles as the precursors. Unique structural features of the as-synthesized materials contributed to promising performance in supercapacitor-related applications.

References